

Rupture Model of the 5 April 2024 Tewksbury, New Jersey, Earthquake Based on Regional *Lg*-Wave Data

Sangwoo Han¹, Won-Young Kim², Jun Yong Park¹, Min-Seong Seo¹, and YoungHee Kim^{*1}

Abstract

On 5 April 2024, an earthquake of magnitude 4.8 occurred in Tewksbury, New Jersey. It was the largest instrumentally recorded event since 1900 in New Jersey and southern New York. Millions of people around New York City, ~65 km east-northeast of Tewksbury, felt the shaking from the mainshock, but the epicentral area experienced no known significant property damages. We determine the focal mechanism, which is oblique faulting, and retrieve the *Lg*-wave relative source time functions (RSTFs) from the stations at regional distances to understand rupture processes and ground motions. Our fault-slip models well explain azimuthal variations of the RSTFs. The models show the rupture propagating toward the east-northeast (~50° to 60°), not along the fault strike. The slip distribution on the nodal plane striking north and dipping to the east shows a slip area of 1.1 km radius with the rupture propagating down-dip. The down-dip rupture may account for the observed lack of strong shaking in the epicentral area.

Cite this article as Han, S., W.-Y. Kim, J. Y. Park, M.-S. Seo, and Y. Kim (2024). Rupture Model of the 5 April 2024 Tewksbury, New Jersey, Earthquake Based on Regional *Lg*-Wave Data, *The Seismic Record*, **4**(3), 214–222, doi: [10.1785/0320240020](https://doi.org/10.1785/0320240020).

Supplemental Material

Introduction

On 5 Friday April 2024, at 10:23 a.m. (EDT), a moderate earthquake of moment magnitude M_w 4.8 (U.S. Geological Survey [USGS]) occurred at Tewksbury Township in northwestern New Jersey, United States (Fig. 1a). The ground motion reached the maximum intensity VI on the modified Mercalli intensity (MMI) scale, and over 5300 residents up to a distance of 25 km from the epicenter reported intensity V. Millions of people around the metropolitan New York City, about 65 km northeast from the epicenter felt intensity IV shaking. The earthquake is the largest instrumentally recorded event since 1900 in New Jersey (Stover and Coffman, 1993). The mainshock was preceded by a foreshock of m_{bLg} 2.2 on 14 March 2024 and followed by 150 aftershocks with magnitudes > 1.0 until 10 May 2024. About 7.5 hr after the mainshock, the largest aftershock occurred (M_w 3.7; USGS). The Community Internet Intensity Map received over 183,000 responses from the public though the “Did You Feel It?” (DYFI) website maintained by the USGS (Wald et al., 2011). The intensity is II around Washington D.C., ~300 km southwest of the epicenter, whereas an intensity of III is reported around White Mountains, New Hampshire, ~450 km northeast of the epicenter. Hence, there is a sense of

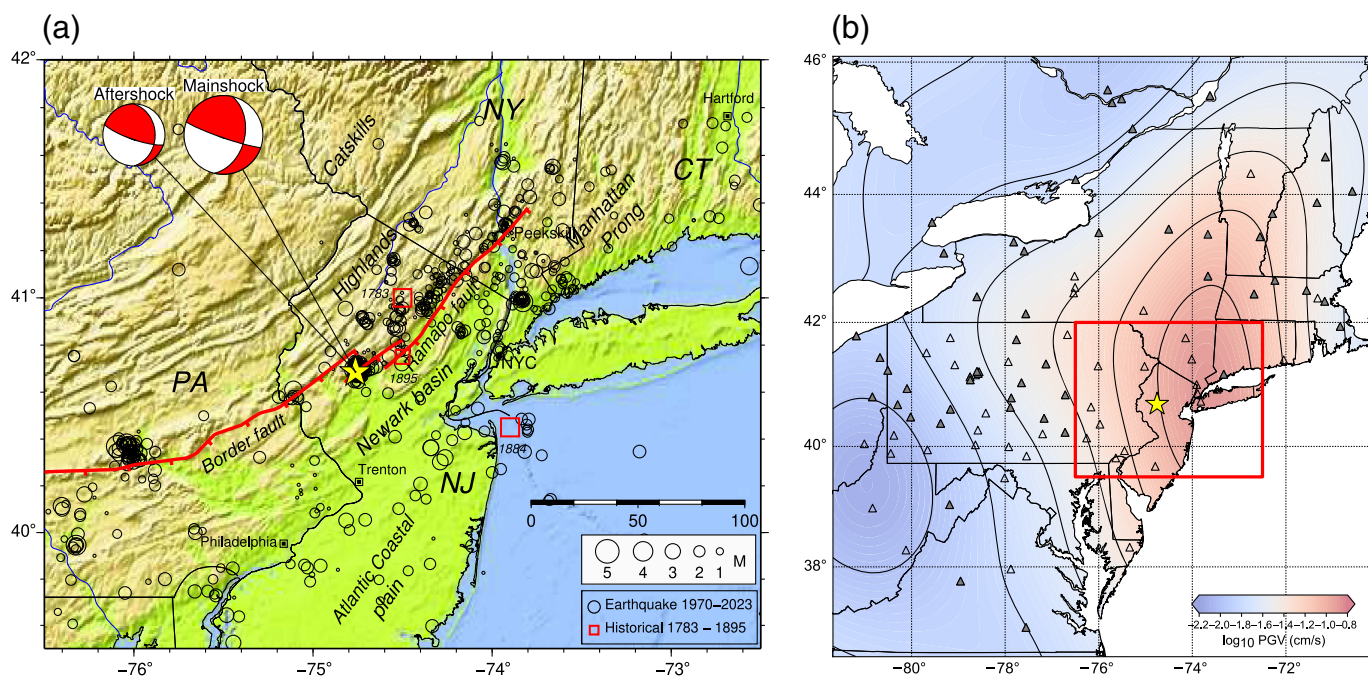
higher intensity observations toward the northeast than the opposite southwest direction. The observed peak ground velocity (PGV) distribution of the mainshock shown in Figure 1b is consistent with the intensity reports; that is, higher PGV values are distributed along the east-northeast direction.

Tewksbury Township is a leisurely rural hamlet located in the foothills of the New Jersey Highlands (Fig. 1a). Although the well-known Ramapo fault system runs close to the area with a northeast trend, the focal mechanism suggests no correlation with the fault system (Fig. 1a; Aggarwal and Sykes, 1978). Although there are no large population centers within 10 km of the epicenter, an intensity VII is expected for the M_w 4.8 event within a distance of ~10 km from the magnitude–intensity

1. School of Earth and Environmental Sciences, Seoul National University, Seoul, Republic of Korea, <https://orcid.org/0000-0001-5832-7127> (SH); <https://orcid.org/0000-0003-2244-0210> (JYP); <https://orcid.org/0000-0001-7043-8938> (M-SS); <https://orcid.org/0000-0002-1111-632X> (YHK); 2. Lamont-Doherty Earth Observatory of Columbia University, Palisades, New York, U.S.A., <https://orcid.org/0000-0002-0005-9681> (W-YK)

*Corresponding author: youngkim@snu.ac.kr

© 2024. The Authors. This is an open access article distributed under the terms of the CC-BY license, which permits unrestricted use, distribution, and reproduction in any medium, provided the original work is properly cited.



relationship established in the central and eastern United States (Boyd and Cramer, 2014). However, even maximum intensity VI was hardly reported with significant property damages, but minor damages, such as cracked walls and objects being thrown from shelves. So far, no surface trace of faulting has been reported for this shallow earthquake of ~ 5 km depth.

Therefore, clear focusing of ground motion toward the northeast as manifested by waveform data and PGV (Fig. S1, available in the supplemental material to this article, Fig. 1b) and relatively low near-field strong ground motion excitation is puzzling; perhaps an unusual rupture process may have taken place. The site effects are also an important factor contributing to ground shaking. However, we found no correlation between known site effect distribution and the felt intensity around our study area (McNamara *et al.*, 2015). In addition to these questions, reported focal mechanisms and our own analysis given in the next section indicate that the observed directional ground motion makes an angle of $\sim 45^\circ$ – 50° to the strikes of both nodal planes (NPs) of this oblique faulting event.

This report aims to investigate the detailed rupture process of the mainshock to answer the aforementioned questions. Because of the lack of local stations—only four stations within 100 km, we will employ the empirical Green's function (EGF) approach and utilize regional L_g waves in retrieving relative source time functions (RSTFs).

Figure 1. (a) Topographic map showing a mainshock (yellow star) and seismicity (open circles) across geological units from west-northwest to east-southeast: Catskills, Highland, Newark basin, and Atlantic Coastal plain. Ramapo fault trending northeast runs through the epicentral area toward Peekskill, New York (NY) (red lines). Border faults between the geologic units—Highland and Newark basin continue southwest from the epicenter through Pennsylvania (PA). Three large known historical earthquakes, 30 November 1783 M 5.3 New Jersey, 1 September 1895 M 4.1 New Jersey, and 10 August 1884 M 5.5 New York, are plotted by red squares. The 2024 Tewksbury earthquake is ~ 20 km west of the 1895 earthquake. (b) Contour map showing mainshock peak ground velocity (PGV) measured on transverse-component records filtered at 0.3–10 Hz. Stations used for the PGV estimation and L_g relative source time function (RSTF) analysis are plotted as open and gray triangles, respectively.

Focal Mechanism and Depth of the Mainshock and the Largest Aftershock

The regional waveform-based focal mechanism solution of the mainshock reported by the USGS showed oblique thrust faulting with a significant strike-slip component at 7 km depth and M_w 4.76 (Table 1). Global Centroid Moment Tensor (Global CMT) solution (Ekström *et al.*, 2012) indicated M_w 4.7 strike-slip event at a fixed depth of 12 km (Table 1). To reconcile the two different focal mechanisms and focal depths reported, we carried out waveform modeling using the frequency-wave-number integration method for the focal mechanism inversion (Saikia, 1994). We employed a crustal velocity model that has

Table 1

Focal Mechanism Parameters Reported by the U.S. Geological Survey (USGS), Global Centroid Moment Tensor (Global CMT), and This Study

	Nodal Plane 1 (NP1)			Nodal Plane 2 (NP2)			M_w^*	M_0 (N·m)	Depth (km)
	Strike (°)	Dip (°)	Rake (°)	Strike (°)	Dip (°)	Rake (°)			
USGS	11	45	158	117	75	47	4.76	1.729×10^{16}	7
Global CMT	10	75	141	112	53	19	4.7	1.45×10^{16}	12
This study (mainshock)	13 ± 0.9	45 ± 4.0	172 ± 1.3	109 ± 0.6	84 ± 0.6	45 ± 4.0	4.84	2.01×10^{16}	5
This study (EGF)	359 ± 0.9	32 ± 1.2	157 ± 3.1	109 ± 1.5	78 ± 2.0	60 ± 0.6	3.82	5.95×10^{14}	7

Uncertainties of the fault parameters are rough estimates from the constrained depth and ± 1 km depths; hence, they are standard deviations of three values. M_0 , seismic moment.

* M_w is moment magnitude, which is defined by $M_w = \frac{2}{3} \log_{10} M_0 [\text{N} \cdot \text{m}] - 6.033$.

been used to locate earthquakes in the southern New York and northern New Jersey regions (Yang and Aggarwal, 1981). Observed waveforms from a dozen stations at 78–394 km distances are modeled. Period bands of 10–33 and 6.7–20 s were used to process waveforms depending on the epicentral distances. We determined focal mechanism parameters (strike, dip, rake, and seismic moment) using a grid search under a constrained deviatoric moment tensor (e.g., Kim *et al.*, 2010). The best-fitting double-couple parameters are listed in Table 1, with the moment magnitude of M_w 4.84. Focal depth is constrained by waveform inversion and by searching depths that maximize variance reduction (VR). The focal depth is fairly well constrained between 3 and 8 km, with peak VR at 5 km.

We followed the same procedure as the mainshock to constrain the focal mechanism and depth for the largest aftershock. We obtained M_w 3.82 for the aftershock. The focal mechanism solution is nearly identical to that of the mainshock with a slightly higher thrust component (Fig. 1a; Table 1), and the waveform data fit best with a slightly deeper depth of 7 ± 2 km. Our moment magnitude (M_w 4.84) for the mainshock is about 0.08–0.14 magnitude units greater than those reported by USGS and Global CMT. The shallow focal depth of 5 km constrained in our solution can account for this difference.

EGF Analysis with Regional *Lg* RSTFs

Regional *Lg*-wave RSTFs

We employed an EGF method to retrieve the RSTF of the mainshock (e.g., López-Comino *et al.*, 2012; Seo *et al.*, 2022) at stations of distances from 132 to 555 km (Fig. 1b). The largest aftershock, which has a common focal mechanism and is located ~ 1 km from the mainshock, is used as the EGF

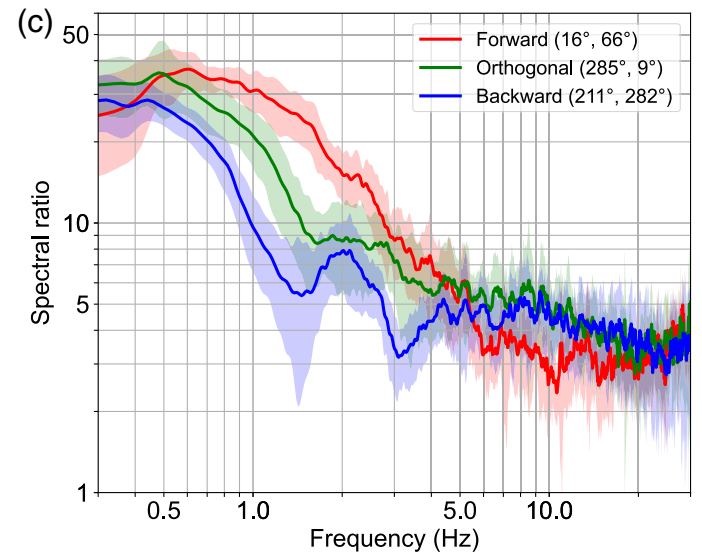
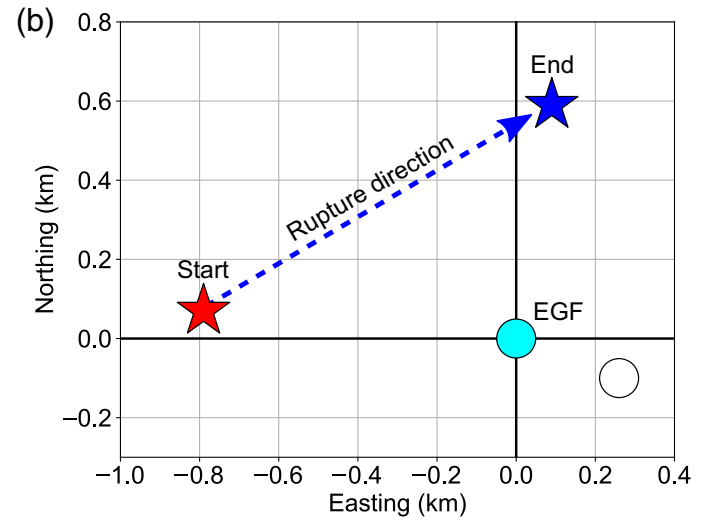
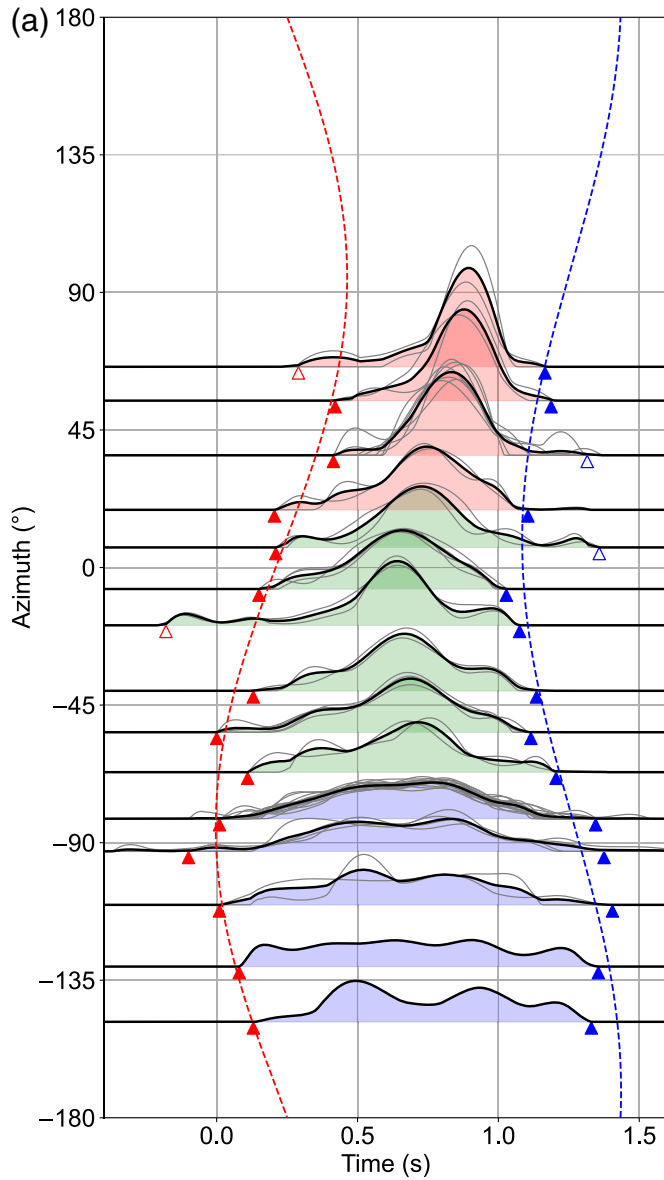
event (Fig. 1a, Fig. S1). We used data from 52 broadband stations covering an azimuth range from -149° to 66° (clockwise direction). The waveforms are dominated by the *Lg* wave (Campillo *et al.*, 1984). We used *Lg* waves on transverse-component records in the time window of 5 s before and 15 s after the arrival at an apparent group velocity of 3.6 km/s, filtered at 0.3–3 Hz.

The *Lg* RSTFs were obtained by aligning the waveforms of the EGF and the mainshock in the same time window starting from the origin times of each event rather than using phase arrival times or cross-correlation times (origin-time preserved RSTF; Han *et al.*, 2024). Offset times in the RSTFs, which reflect travel-time differences between the mainshock and EGF, were used to determine the relative locations of the mainshock rupture against the EGF location. We used projected-Landweber deconvolution with constraints of positivity and causality, allowing us to capture the approximate start and end times of the source pulse (Bertero *et al.*, 1997).

Although the *Lg* RSTFs do not have good depth constraints, they preserve source properties in the azimuthal direction (Gallegos and Xie, 2020; Han *et al.*, 2024). The *Lg* RSTFs with the
$$\text{VR} \left(\left[1 - \frac{\sum_i (\text{target}(t) - \text{EGF}(t) * \text{RSTF}(t))^2}{\sum_i \text{target}(t)^2} \right] \times 100\% \right)$$
 greater than 50% were selected, normalized so that each integrated area is equal to the seismic moment, and stacked in 15° azimuth bins to enhance the robustness of their shapes (Fig. 2a).

Rupture directivity in the time domain

The travel-time differences caused by the offsets between the two events are reflected as time shifts in the RSTFs. The start and end times of the RSTFs are used to infer the horizontal locations of the start and end points of the rupture relative



to the EGF location set as the origin. The start and end points estimate the rupture extent on the horizontal plane. We measured the start and end times of the stacked *Lg* RSTFs at various azimuths and used them to estimate the horizontal locations (e_0, n_0) and time delays (Δt_0) of the mainshock's rupture start and end (Fig. 2a). A least-squares minimization of the apparent times of RSTFs is performed by the grid search as

$$\tau_i(\phi_j) = \Delta t_i - \frac{\sqrt{e_i^2 + n_i^2} \cos \phi_j}{V_s}, \quad (1)$$

in which $\tau_i(\phi_j)$ is the theoretical apparent time of the i th candidate location at the j th *Lg* RSTF for which azimuth is ϕ_j , and

Figure 2. (a) *Lg* RSTFs stacked in a 15° azimuth bin (thick black lines) and individual RSTFs (thin gray lines). The start and end of the RSTFs are represented by red and blue triangles, respectively, and their anomalous values by open triangles of the same colors. The best-fitting sinusoidal curves for their variations are indicated by red and blue dashed lines. The RSTFs are colored along the rupture forward (red), orthogonal (green), and backward (blue) directions. (b) Rupture initiation (red star) and termination points (blue star) on the horizontal plane. A dashed blue arrow indicates an inferred rupture direction. The location difference between the mainshock and empirical Green's function (EGF) event obtained from the relocation is indicated by an open circle. (c) Stacked spectral ratios along the rupture forward, orthogonal, and backward directions with a standard deviation of each stacked ratio (shaded area) with the corresponding color with (a). Each direction consists of stations within each direction $\pm 45^\circ$ azimuth range.

Δt_i is the delay of the rupture start (or end) time. The i th candidate location is indicated by (e_i (positive to the east), n_i (positive to the north)), and $\sqrt{e_i^2 + n_i^2}$ is the distance of the i th candidate location from the EGF. $V_S = 3400$ m/s is used for the S-wave velocity at the source region.

The estimates of the rupture start and end points are (−790 m, 70 m) and (90 m, 590 m), and their corresponding times are 0.23 and 1.26 s, respectively (Fig. 2b). Therefore, the mainshock rupture propagated with a horizontally projected length of ∼1000 m, mostly extended toward the east-northeast (∼59°) in ∼1.0 s (Fig. 2b). The rupture propagating toward opposite direction cannot be precisely estimated due to resolution limits imposed by the limited azimuthal coverage (Abercrombie *et al.*, 2017).

Rupture directivity in the frequency domain

Because we observed variations in the duration of RSTFs, we further utilized the spectral ratios of the mainshock and the largest aftershock as an EGF pair to identify rupture directivity in the frequency domain (Prieto *et al.*, 2009). We stacked the spectral ratios for stations used in the RSTF analysis along three directions to represent directivity—forward, orthogonal, and backward of the mainshock rupture direction presumed in RSTF analysis (Fig. 2c). The higher and lower amplitudes along the forward and backward direction in high frequency, respectively, show strong directivity with unilateral rupture characteristics (e.g., Calderoni *et al.*, 2017; Trugman, 2022).

Rupture Model

1D fault-slip inversion

We inverted the L_g RSTFs to determine the spatiotemporal slip distribution of the rupture. We constructed a 1D line source model for the inversion modeled by N -point sources with an interval of 100 m along the fault strike directions (e.g., Stich *et al.*, 2020; Han *et al.*, 2024). The inversion was performed with a fixed velocity of the rupture front starting from the hypocenter location described in the previous section. This was done under the assumption that the slip occurs only at the rupture front (i.e., pulse-like rupture), as shown in the following equation:

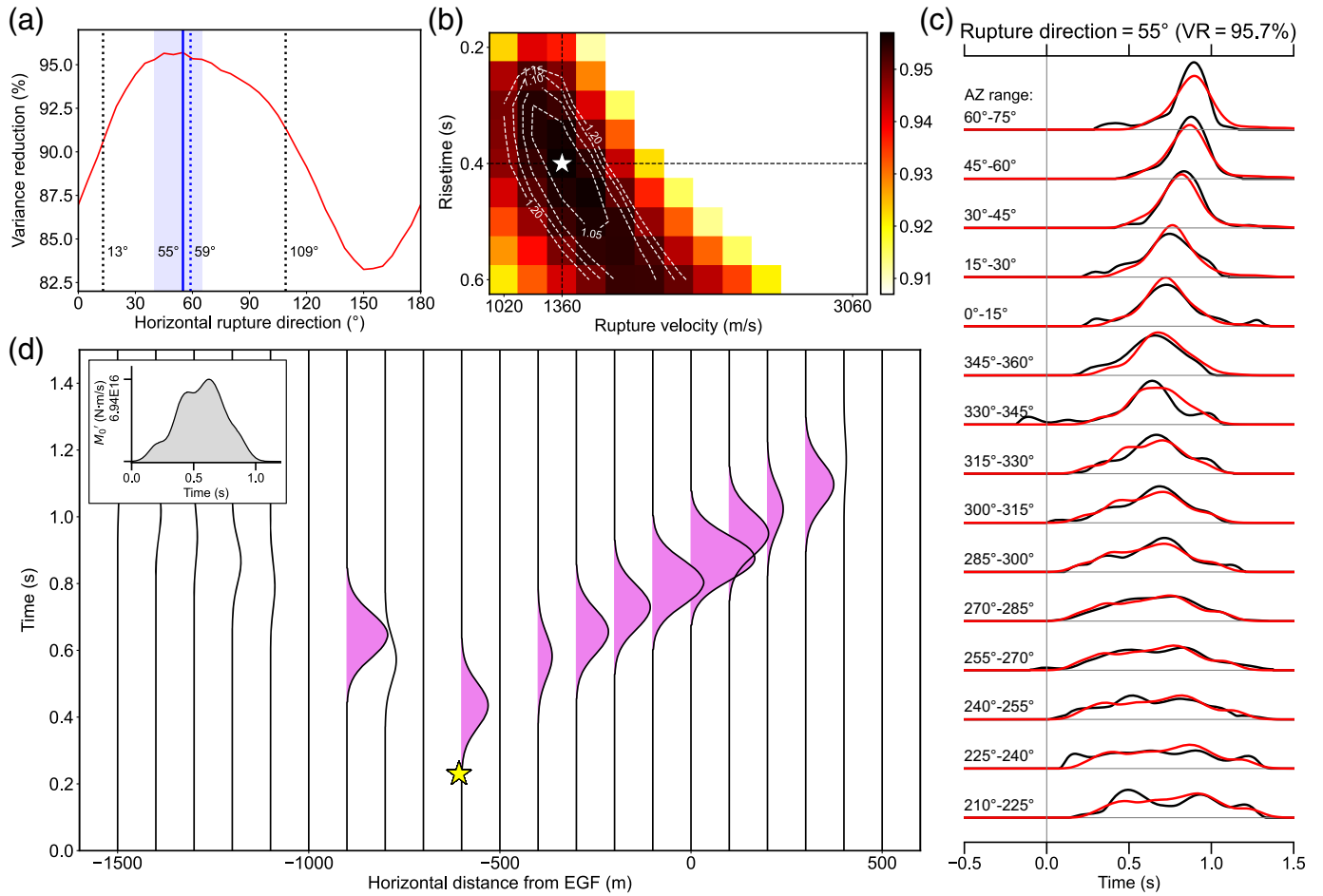
$$\text{RSTF}_j(t) = \sum_i^N A(d_i) s\left(t - t_i + \frac{d_i \cos \Delta \phi_j}{V_S}, t_r\right), \quad (2)$$

in which $\text{RSTF}_j(t)$ is the j th L_g RSTF; $A(d_i)$ is the amplitude of the slip-rate function being solved in the inversion; $s(t, t_r)$ is the slip-rate function at each point source, which is assumed to be a

Gaussian-shaped pulse, in which t_r is the risetime of each sub-fault; $\Delta \phi_j = \phi_j - \phi_r$ is the angle between the fault strike (or rupture) direction (ϕ_r) and the j th azimuth bin (ϕ_j). The risetime indicates the duration of the slip from a point source along the fault (Heaton, 1990). In this case, the rupture time t_i at location d_i is defined as $t_i = t_0 + \frac{|d_i - d_0|}{V_R}$, in which t_0 is the origin time, d_0 is a straight-line distance from the EGF to the mainshock hypocenter along the strike direction, and V_R is the apparent rupture velocity as the horizontal component of rupture velocity on the fault plane. This equation is a reformulated version for the origin-time preserved RSTFs, considering the EGF location as the coordinate reference point instead of the hypocenter used in the usual slip inversion.

Preliminary inversion was performed for two strike directions of 13° (NP1) and 109° (NP2) by nonnegative least-squares minimization (Lawson and Hanson, 1974) while searching for the optimal V_R and t_r that maximize the VR (Fig. S2). Results show that this simple 1D rupture model, constrained to propagate along the strike direction, cannot fully capture the observed RSTF variability across different azimuths (Figs. S2c,d). Therefore, we performed the inversion by varying ϕ_r from 0° to 180° in 5° increments, considering the directivity associated with rupture propagation in the dip direction. We investigated the best-fit V_R and t_r for each rupture direction. The VR is significantly improved to 95.7% at $\phi_r = 55^\circ$, with its uncertainty range of 40°–65° estimated at $1.1 \times$ optimum misfit (Fig. 3a,c). This ϕ_r is quite close to the direction estimated from rupture start and end points (∼59°; Figs. 2b, 3a). When we used V_R of 1.36 km/s (∼0.4 × V_S) and t_r of 0.4 s at $\phi_r = 55^\circ$ (Fig. 3b), the slip distribution reveals that the rupture propagated forward for 1000 m in ∼1 s (Fig. 3d). A slip pulse at −900 m, as shown in Figure 3d, could be attributed to either backward rupture propagation or a small subevent.

To infer vertical components of the rupture direction, which is not observable from horizontal measurements of the L_g RSTFs, we assume the rupture direction is within the fault plane of two NPs. Then, we project the horizontal direction $\phi_r = 55^\circ$ onto the NPs. We estimate true rupture velocity on the fault plane by accounting for the apparent velocity reduction by $\cos \delta$ in the dip direction, which is reflected in $V_R = 0.4 \times V_S$. As the results indicate, the inverted rupture velocities for NP1 and NP2 are ∼0.5 × V_S and ∼3.1 × V_S toward the down-dip and up-dip directions, respectively. The steep dip of 84° results in an abnormally fast (super shear) rupture velocity for NP2, whereas the value for NP1 is acceptable.



2D fault-slip inversion

Although our 1D model adequately explains observed RSTF variations providing several rupture properties, such as rupture direction, length, and velocity, we further performed 2D inversion to infer the rupture area. Equation (2) for the 1D model is modified for the 2D slip on the fault plane as follows:

$$\text{RSTF}_j(t) = \sum_i \sum_k A(x_i, z_k) s\left(t - t_{ik} + \frac{x_i \cos \Delta\phi_j + z_k \cos \delta \cos(\Delta\phi_j + 90^\circ)}{V_S}, t_r\right), \quad (3)$$

in which $A(x_i, z_k)$ is the amplitude of the slip-rate function of a point source for which the location is x_i (positive to the strike), z_k (positive to the up-dip) on the fault plane; the rupture time t_{ik} at location (x_i, z_k) is defined as $t_{ik} = t_0 + \frac{\sqrt{(x_i - x_0)^2 + (z_k - z_0)^2}}{V_R}$, in which (x_0, z_0) is a projection of the horizontal location of the mainshock hypocenter (e, n) on the fault plane (Fig. 4c), and

Figure 3. One-dimensional fault-slip inversion result. (a) Variance reductions (VRs) depend on rupture directions, which are indicated by a red line. The optimal rupture direction of 55° is indicated by a solid blue line with the shaded area indicating its uncertainty range. Dotted black lines represent two strike directions of the determined focal mechanism; a dotted blue line indicates the rupture direction estimated from the start and end of the rupture (Fig. 2b). (b) VRs at the rupture direction of 55° in searching for apparent rupture velocity and risetime. A star indicates the apparent rupture velocity and risetime that maximize VR. (c) Comparison between the *Lg* RSTFs (black) and synthetics (red) calculated by the 1D slip model that maximizes VR. (d) Slip distribution along the rupture direction of 55°. Slip-rate function at 100 m intervals is plotted with its amplitude scaled to seismic moment (pink representing >3% total moment). A yellow star indicates the start position of the mainshock. The inset shows the moment rate function (source time function).

V_R is the true rupture velocity on the fault plane; δ is the dip angle of the fault plane. For example, $(e, n) = (-790 \text{ m}, 70 \text{ m})$ is converted as $(x_0, z_0) = (-110 \text{ m}, 1111 \text{ m})$ for NP1 and $(x_0, z_0) = (-770 \text{ m}, -1827 \text{ m})$ for NP2. Here, we also consider the EGF location as the coordinate reference point of $(x_i, z_k) = (0, 0)$,

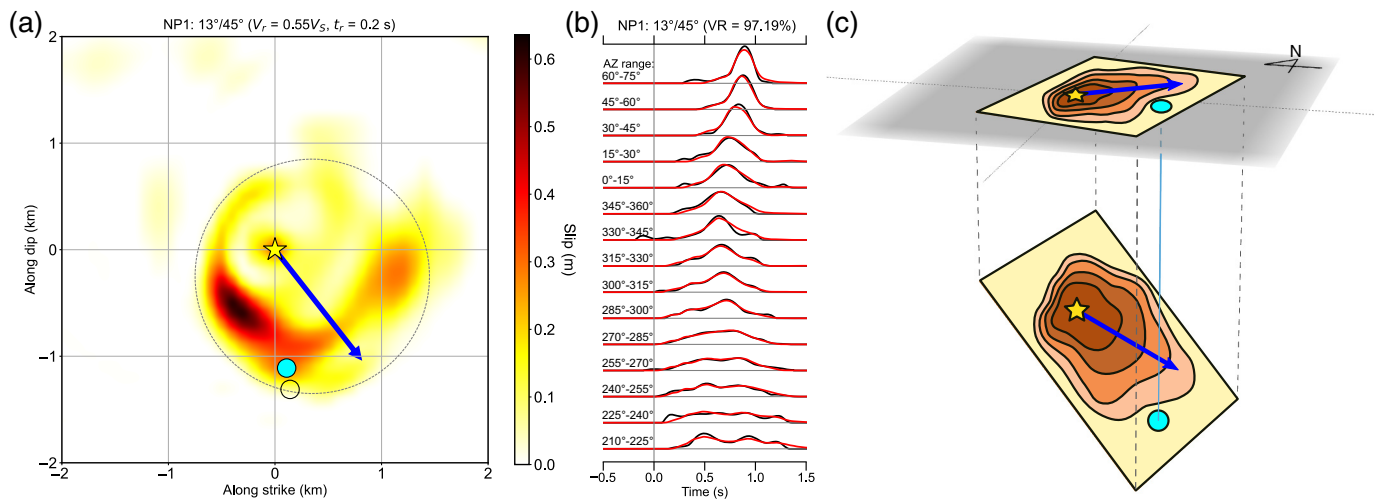


Figure 4. Two-dimensional fault-slip inversion result. (a) Slip distribution on nodal plane 1 (NP1; strike = 13° and dip = 45°). A blue arrow indicates the 1D inversion result showing the rupture direction and its extent projected on the fault plane. EGF locations obtained by the start time of the RSTF and by the double-difference relocation are represented by cyan and open circles, respectively. A slip area of a radius of 1.1 km is indicated by a dotted gray circle. (b) Comparison between the *Lg* RSTFs (black) and synthetics (red). (c) Schematic illustration of the mainshock rupture process on NP1 and its projection on the horizontal plane. The mainshock hypocenter and EGF events are plotted as a yellow star and a cyan circle, respectively.

assuming that the EGF event occurred on the mainshock fault plane. The rupture propagation in the dip direction is multiplied by $\cos \delta$ considering the projection to the horizontal plane.

We constructed 2D model space on a 4×4 km fault plane centered at (x_0, z_0) with a grid spacing of 100 m in both x and z directions. We implemented linear regularization for spatially adjacent values of $A(x, z)$ to avoid ill-posed problems during the inversion (Everett, 2013). Based on the L-curve test result, we selected a regularization parameter $\lambda = 400$. The optimal rupture velocities were found to be $0.55 \times V_S$ for NP1 and $1.75 \times V_S$ for NP2, at a risetime of 0.2 s.

Figure 4a shows slip distribution on NP1 with the rupture direction constrained from 1D inversion (blue arrow). High-slip density is southeast to east, which is somewhat shifted from the expected direction along the blue arrow starting from the hypocenter. This might be due to the lack of station coverage in the southeastern quadrant (Fig. 1b) and the large model space of 2D inversion cells with 1600 elements (40×40). The rupture direction is robustly constrained by the 1D inversion (Fig. 3d), whereas the 2D inversion yields reasonable estimates of the main rupture area, clearly indicating a circular rupture of radius ~ 1.1 km (Fig. 4a). A static stress drop of ~ 6.6 MPa can be estimated from the source radius using $\Delta\sigma = (7/16)M_0/r^3$ (Eshelby, 1957).

We note that high-slip density on the fault plane is predominantly distributed in the down-dip direction, and the area extending the farthest from the hypocenter corresponds to the forward direction of the 1D rupture. The projected EGF on the fault plane is situated at the periphery of the slip area (Fig. 4a, cyan circle), indicating that the largest aftershock occurred at

the edge of the mainshock rupture. Synthetic *Lg* RSTFs are nearly identical to observations, indicating the robustness of our model (Fig. 4b). For NP2, the model shows overly extended slip distribution (>5 km) in the fault dip direction with anomalously fast (super shear) rupture speed (Fig. S3).

Discussion

Progressive rupture modeling

We inverted *Lg* RSTFs (Fig. 2a) using three progressively evolved models. (1) By utilizing the start and end times of the origin-time preserved *Lg* RSTFs (Fig. 2a), we obtained a first-order solution for the mainshock rupture that propagated for ~ 1 km toward east-northeast ($\sim 59^\circ$) in ~ 1 s. (2) Using the 1D rupture model (Fig. 3d), we obtained a dominant rupture direction of 55° from a linear slip distribution. The 1D inversion is robust due to its simple parameterization. (3) Through 2D modeling, we obtained a slip distribution on the fault plane (Fig. 4a), providing a realistic rupture dimension and rupture velocity. The slip distribution favors NP1 as the rupture plane and, hence, the rupture propagation in the down-dip direction.

Which NP?

Assuming that the EGF and the mainshock occurred on the same fault plane, the relative horizontal location of the EGF to the mainshock suggests that the EGF is 0.9 km deeper than the mainshock. The depth difference is consistent with the result of the moment tensor inversion, showing ~ 1 km deeper for the EGF than the mainshock. The EGF and mainshock relocated by the double-difference method (Waldhauser and Ellsworth, 2000) using body-wave phases indicated that the EGF is 1050 m east, 170 m south, and 830 m deeper than the mainshock (Figs. 2b, 4a).

If we consider an NP-striking east-southeast (109°) and dipping steeply to the southwest (84° ; NP2) as the fault plane, the depth of the EGF becomes ~ 2 km shallower than the mainshock hypocenter, which is inconsistent with the waveform modeling and relocation results (Fig. S3). The anomalously fast rupture velocity ($\sim 1.75 \times V_S$) is obtained for rupture propagation toward the up-dip direction that cannot be easily reconciled.

Figure 4c summarizes the rupture process on the fault plane based on our inversion result. It shows the horizontal rupture length of ~ 1 km in the direction of 55° – 59° . Based on the fault geometry of NP1, this corresponds to the rupture length of ~ 1.23 km with a rupture velocity of $\sim 0.55 \times V_S$ in the down-dip direction.

A lack of near-field strong motion?

The rupture progressing down-dip (Fig. 4c) might have resulted in the lack of strong shaking exceeding MMI VI, which is usually expected for a moment magnitude of 4.8 events in the near-field around the epicenter (Fig. S4). Only six felt reports show VI, which contrasts with the frequent VI region near the epicenter of the 2003 Central Virginia earthquake with a lower M_w of 4.3 and a deeper focal depth of 10 km (Kim and Chapman, 2005). The high PGV values and the intensity values of IV broadly felt in the east-northeast direction, where New York City is located, must have been due primarily to the mainshock rupture directivity at 40° – 65° direction (Fig. 1b).

Conclusions

We summarize our proposed rupture model for the 2024 Tewksbury, New Jersey, earthquake as follows: the rupture initiated at 5 km depth on the fault plane trending north–south and dipping moderately to the east. It propagated down-dip for ~ 1 s with a speed of 1.87 km/s and in azimuth of 55° – 59° . The

mainshock rupture area indicates a circular rupture with a radius of ~ 1.1 km that yields a static stress drop of ~ 6.6 MPa. The proposed rupture model accounts for the lack of maximum intensity greater than V (MMI) at the epicenter and focused broad-intensity IV areas and high-PGV values toward the northeast.

Data and Resources

Focal mechanism solutions from the U.S. Geological Survey (USGS; <https://earthquake.usgs.gov/earthquakes/eventpage/us7000ma74/moment-tensor>) and Global Centroid Moment Tensor (Global CMT; <https://www.globalcmt.org/>) were used. Seismic intensity estimated by “Did You Feel It?” (DYFI; <https://earthquake.usgs.gov/earthquakes/eventpage/us7000ma74/dyfi/intensity>) was used. Broadband waveforms and station metadata were obtained via the International Federation of Digital Seismograph Networks (FDSN) web services (www.fdsn.org/webservices). Seismic Analysis Code (SAC; <https://ds.iris.edu/ds/nodes/dmc/software/downloads/sac/>) and ObsPy (v.1.4.0; <https://docs.obspy.org/>) were used for data processing; and Basemap (v.1.4.1; <https://matplotlib.org/basemap/stable/>) and Generic Mapping Tools (GMT, v.6.3.0; <https://www.generic-mapping-tools.org>) for making geological maps. Past seismicity in the eastern United States was obtained from the Advanced National Seismic System (ANSS) Comprehensive Earthquake Catalog (<https://earthquake.usgs.gov/data/comcat/>). All websites were last accessed in May 2024. The supplemental material includes four figures.

Declaration of Competing Interests

The authors acknowledge that there are no conflicts of interest recorded.

Acknowledgments

This work was supported by the National Research Foundation of Korea (2022R1A2C1003006 and 2022R1A5A1085103). W.-Y. Kim received support from the Consortium for Monitoring, Technology, and Verification under the Department of Energy National Nuclear Security Administration Award Number DE-NA0003920. The authors thank Editor-in-Chief Keith D. Koper and Associate Editor Pascal Audet for their support and appreciate Rachel E. Abercrombie and one anonymous reviewer for their thoughtful comments and constructive reviews.

References

Abercrombie, R. E., P. Poli, and S. Bannister (2017). Earthquake directivity, orientation, and stress drop within the subducting plate at

- the Hikurangi margin, New Zealand, *J. Geophys. Res.* **122**, 10,176–10,188, doi: [10.1002/2017JB014935](https://doi.org/10.1002/2017JB014935).
- Aggarwal, Y. P., and L. R. Sykes (1978). Earthquakes, faults, and nuclear power plants in southern New York and northern New Jersey, *Science* **200**, 425–529, doi: [10.1126/science.200.4340.425](https://doi.org/10.1126/science.200.4340.425).
- Bertero, M., D. Bindi, P. Boccacci, M. Cattaneo, C. Eva, and V. Lanza (1997). Application of the projected Landweber method to the estimation of the source time function in seismology, *Inverse Prob.* **13**, no. 2, 465–486, doi: [10.1088/0266-5611/13/2/017](https://doi.org/10.1088/0266-5611/13/2/017).
- Boyd, O. S., and C. H. Cramer (2014). Estimating earthquake magnitudes from reported intensities in the central and eastern United States, *Bull. Seismol. Soc. Am.* **104**, no. 4, 1709–1722, doi: [10.1785/0120120352](https://doi.org/10.1785/0120120352).
- Calderoni, G., A. Rovelli, and R. Di Giovambattista (2017). Rupture directivity of the strongest 2016–2017 central Italy earthquakes, *J. Geophys. Res.* **122**, no. 11, 9118–9131, doi: [10.1002/2017JB014118](https://doi.org/10.1002/2017JB014118).
- Campillo, M., M. Bouchon, and B. Massinon (1984). Theoretical study of the excitation, spectral characteristics, and geometrical attenuation of regional seismic phases, *Bull. Seismol. Soc. Am.* **74**, no. 1, 79–90, doi: [10.1785/BSSA0740010079](https://doi.org/10.1785/BSSA0740010079).
- Ekström, G., M. Nettles, and A. M. Dziewoński (2012). The global CMT project 2004–2010: Centroid-moment tensors for 13,017 earthquakes, *Phys. Earth Planet. In.* **200**, 1–9, doi: [10.1016/j.pepi.2012.04.002](https://doi.org/10.1016/j.pepi.2012.04.002).
- Eshelby, J. D. (1957). The determination of the elastic field of an ellipsoidal inclusion, and related problems, *Proc. Roy. Soc. Lond.* **241**, no. 1226, 376–396, doi: [10.1098/rspa.1957.0133](https://doi.org/10.1098/rspa.1957.0133).
- Everett, M. E. (2013). *Near-Surface Applied Geophysics*, Cambridge University Press, New York.
- Gallegos, A., and J. Xie (2020). A multichannel deconvolution method to retrieve source–time functions: application to the regional Lg wave, *Geophys. J. Int.* **223**, no. 1, 323–347, doi: [10.1093/gji/ggaa303](https://doi.org/10.1093/gji/ggaa303).
- Han, S., W.-Y. Kim, H. Lim, Y. O. Son, M.-S. Seo, J. Y. Park, and Y. Kim (2024). Resolving multi-stage rupture process of the 2021 Mw 4.9 Offshore Jeju Island earthquake from relative source time functions, *Geophys. Res. Lett.* **51**, no. 3, e2023GL106059, doi: [10.1029/2023GL106059](https://doi.org/10.1029/2023GL106059).
- Heaton, T. H. (1990). Evidence for and implications of self-healing pulses of slip in earthquake rupture, *Phys. Earth Planet. In.* **64**, no. 1, 1–20, doi: [10.1016/0031-9201\(90\)90002-F](https://doi.org/10.1016/0031-9201(90)90002-F).
- Kim, W.-Y., and M. Chapman (2005). The 9 December 2003 central Virginia earthquake sequence: A compound earthquake in the central Virginia seismic zone, *Bull. Seismol. Soc. Am.* **95**, no. 6, 2428–2445, doi: [10.1785/0120040207](https://doi.org/10.1785/0120040207).
- Kim, W.-Y., H. Choi, and M. Noh (2010). The 20 January 2007 Odaesan, Korea, earthquake sequence: Reactivation of a buried strike-slip fault? *Bull. Seismol. Soc. Am.* **100**, no. 3, 1120–1137, doi: [10.1785/0120090069](https://doi.org/10.1785/0120090069).
- Lawson, C. L., and R. J. Hanson (1974). *Solving Least Squares Problems*, Prentice Hall, New York, New York.
- López-Comino, J. Á., F. D. L. Mancilla, J. Morales, and D. Stich (2012). Rupture directivity of the 2011 Mw 5.2 Lorca earthquake (Spain), *Geophys. Res. Lett.* **39**, no. 3, doi: [10.1029/2011GL050498](https://doi.org/10.1029/2011GL050498).
- McNamara, D. E., W. J. Stephenson, J. K. Odum, R. A. Williams, and L. Gee (2015). Site response in the eastern United States: A comparison of VS30 measurements with estimates from horizontal: vertical spectral ratios, *U.S. Geol. Soc. Am.*, Vol. **509**, 67–79, doi: [10.1130/2015.2509\(04\)](https://doi.org/10.1130/2015.2509(04)).
- Prieto, G. A., R. L. Parker, and F. L. Vernon (2009). A Fortran 90 library for multitaper spectrum analysis, *Comput. Geosci.* **35**, no. 8, 1701–1710, doi: [10.1016/j.cageo.2008.06.007](https://doi.org/10.1016/j.cageo.2008.06.007).
- Saikia, C. K. (1994). Modified frequency-wavenumber algorithm for regional seismograms using Filon's quadrature: Modelling of Lg waves in eastern North America, *Geophys. J. Int.* **118**, no. 1, 142–158, doi: [10.1111/j.1365-246X.1994.tb04680.x](https://doi.org/10.1111/j.1365-246X.1994.tb04680.x).
- Seo, M.-S., W.-Y. Kim, and Y. Kim (2022). Rupture directivity of the 2021 ML 2.2 Gwangyang, Korea, microearthquake: Toward resolving high-resolution rupture process of a small earthquake, *Seism. Record* **2**, no. 4, 227–236, doi: [10.1785/0320220030](https://doi.org/10.1785/0320220030).
- Stich, D., R. Martín, J. Morales, J. Á. López-Comino, and F. D. L. Mancilla (2020). Slip partitioning in the 2016 Alboran Sea earthquake sequence (Western Mediterranean), *Front. Earth Sci.* **8**, 587356, doi: [10.3389/feart.2020.587356](https://doi.org/10.3389/feart.2020.587356).
- Stover, C. W., and J. L. Coffman (1993). Seismicity of the United States, 1568–1989 (Revised), *U.S. Geol. Surv. Profess. Paper* 1527, 418 pp., doi: [10.3133/pp1527](https://doi.org/10.3133/pp1527).
- Trugman, D. T. (2022). Resolving differences in the rupture properties of M5 earthquakes in California using Bayesian source spectral analysis, *J. Geophys. Res.* **127**, no. 4, e2021JB023526, doi: [10.1029/2021JB023526](https://doi.org/10.1029/2021JB023526).
- Wald, D. J., V. Quitoriano, C. B. Worden, M. Hopper, and J. W. Dewey (2011). USGS “Did You Feel It?” internet-based macroseismic intensity maps, *Ann. Geophys.* **54**, no. 6, doi: [10.4401/ag-5354](https://doi.org/10.4401/ag-5354).
- Waldhauser, F., and W. L. Ellsworth (2000). A double-difference earthquake location algorithm: Method and application to the northern Hayward fault, California, *Bull. Seismol. Soc. Am.* **90**, no. 6, 1353–1368, doi: [10.1785/0120000006](https://doi.org/10.1785/0120000006).
- Yang, J.-P., and Y. P. Aggarwal (1981). Seismotectonics of northeastern United States and adjacent Canada, *J. Geophys. Res.* **86**, 4981–4998, doi: [10.1029/JB086iB06p04981](https://doi.org/10.1029/JB086iB06p04981).

Manuscript received 5 June 2024
Published online 18 September 2024